Materials Characterization 233 (2026) 116053

Contents lists available at ScienceDirect

Materials Characterization

journal homepage: www.elsevier.com/locate/matchar

The influence of heat treatment on precipitate formation in Scalmalloy®: *In-situ* X-ray diffraction investigation

Fábio Faria Conde [a], André H.G. Gabriel [a], N. Schell [d], J.P. Oliveira [b], Julian A. Avila [c], Eduardo B. da Fonseca [a,e], Éder S.N. Lopes [a,*]

[a] Faculdade de Engenharia Mecânica, Universidade Estadual de Campinas (UNICAMP), 13083-860 Campinas, SP, Brazil
[b] CENIMATi3N, Department of Materials Science, School of Science and Technology, NOVA University Lisbon, Caparica, Portugal
[c] UNESP – São Paulo State University, Campus of São João da Boa Vista, Av. Prof[a] Isette Corrêa Fontão, 505, Jardim das Flores, 13876-750 - São João da Boa Vista, SP, Brazil
[d] Institute of Materials Physics, Helmholtz-Zentrum Hereon, Max-Planck-Str.1, Geesthacht D-21502, Germany
[e] Centro de Tecnologia da Informação Renato Archer, 13069-901 Campinas, SP, Brazil

ARTICLE INFO

Keywords:
PBF-LB
Al alloy
Al-Sc
In-situ XRD
Precipitation
Al_3Sc
Al_6Mn

ABSTRACT

Additive manufacturing offers a novel approach to producing lightweight components with complex geometries. Aluminum alloys, renowned for their low density and high mechanical properties, have emerged as prime candidates for this technology. Aluminum alloys, processed using laser-based powder bed fusion (PBF-LB), have gained significant interest in aerospace, construction, and automotive applications due to their lightweight properties, corrosion resistance, and fine-grained microstructure. Given its recent attention, PBF-LB Scalmalloy® samples were subjected to *in-situ* coupled experiments with heat treatments in a high-energy X-ray diffraction (HEXRD) beamline to collect diffractograms in transmission mode. Subsequently, transmission electron microscopy (TEM) was used to analyze the microstructure deeply and pursue the characterization of the formed precipitates. Results showed finely dispersed precipitates formed, which evolved slowly in lower heat-treatment temperatures, under 325 °C. In contrast, a higher temperature of 400 °C led to coarsening and hardness loss for long treatment periods.

1. Introduction

Scalmalloy® is commonly used to refer to the second generation of Aluminum-Magnesium-Scandium (Al-Mg-Sc) alloys. Developed by Airbus Group Innovations, it is a high-strength aluminum alloy specifically designed for laser-based powder bed fusion (PBF-LB) additive manufacturing (AM). While the 6XXX series aluminum alloys, such as AlSi12, AlSi10Mg, and AlSi7Mg0.3, have been widely used in PBF-LB, they were originally developed for casting processes and are primarily silicon-based [1–3]. In contrast, Scalmalloy® contains significantly lower silicon content and derives its unique properties from the combination of scandium and zirconium with more common alloying elements [4]. Scalmalloy® exhibits a closer compositional resemblance to the 5XXX series of Al-Mg alloys [5]. Research into the effects of scandium on aluminum alloys was initiated in the 1960s and 1970s. However, limited access to these publications and the high cost of scandium at the time hindered further research [6]. It wasn't until around 2000 that new studies began to delve deeper into the impact of this element [7].

Early studies on the influence of scandium in aluminum alloys, such as those by Norman et al. [6] and Royset [7], did not specifically address additive manufacturing, but highlighted the positive effects of scandium on the mechanical properties of aluminum alloys. These studies indicated a eutectic point in the Al-Sc system of around 0.5 wt% scandium at 655 °C. Despite slight variations in the reported eutectic point, these studies consistently highlight the beneficial effects of scandium, particularly at hypereutectic compositions (0.6–0.8 wt%), on the mechanical properties of aluminum alloys. This enhancement is attributed to the formation of Al_3Sc particles during solidification, which contribute to increased strength, grain refinement, and improved weldability [8]. Royset [7] further delineated the temperature range for optimal particle precipitation, a finding widely referenced in subsequent studies on heat treatment.

Many authors investigated the influence of PBF-processing

* Corresponding author.
E-mail address: esnlopes@unicamp.br (É.S.N. Lopes).

https://doi.org/10.1016/j.matchar.2026.116053
Received 5 September 2025; Received in revised form 29 December 2025; Accepted 20 January 2026
Available online 25 January 2026
1044-5803/© 2026 The Authors. Published by Elsevier Inc. This is an open access article under the CC BY license (http://creativecommons.org/licenses/by/4.0/).

parameters and post-heat-treatments on the microstructure and properties of AlMgScZrMn alloys [9–15]. PBF-LB produced a refined microstructure, characterized by a mixture of equiaxed and columnar grains [11,14]. The superior mechanical performance of PBF-LB samples was attributed to a high density of nanoscale Al_3Sc particles and Mn_2Sc precipitates. These precipitates, distributed throughout the microstructure, effectively hindered dislocation motion and twinning, improving strength and ductility [9]. However, identifying and finding these precipitates is difficult, and scarce literature has been published. Furthermore, few papers present X-ray diffraction (XRD) patterns after heat-treatment cycles to verify the presence of other phases and precipitates [16–18]. Most of the published literature brings XRD results without precipitate identification [10,11,14,15] and without a time-related characterization or with the high resolution a synchrotron source can provide. Conventional XRD diffractometers (Cu/Mo-Kα) provide limited resolution ($\Delta 2\theta \approx 0.05$–$0.1^\circ$) with peak overlap at higher angles, while 87 keV synchrotron achieves superior resolution ($\Delta 2\theta \approx 0.001$–$0.01^\circ$) by shifting peaks to lower angles, enabling a more precise phase discrimination. Moreover, the high flux of synchrotron sources allows rapid, bulk-sensitive measurements ideal for *in-situ* studies and trace phase detection [19].

In-situ study using in X-ray and neutron diffraction enables real-time tracking of phase precipitation, lattice strain evolution, and load partitioning in Al alloys with high temporal and structural resolution. The combined techniques uniquely capture the kinetics, morphology, and coherency of nanoscale precipitates during aging and deformation. This multiscale, *in situ* approach provides insights inaccessible to *ex situ* methods, directly linking microstructural evolution to mechanical performance [20].

XRD analysis represents a transformative approach for studying precipitation evolution in metallic alloys, offering distinct advantages over traditional *ex-situ* microscopy analysis [21]. Unlike transmission electron microscopy (TEM), which provides high-resolution images of microstructures after quenching, *in situ* XRD enables real-time monitoring of phase transformations during thermal processing, capturing transient phenomena such as nucleation kinetics and intermediate phase formation that are often lost in *post mortem* samples. This dynamic capability is particularly valuable in precipitation-hardening alloys such as maraging steels [22], or even Al-Sc, where precipitation sequences—such as Guinier-Preston zones progressing to stable θ phases—involve rapid, non-equilibrium states influenced by heating rates and deformation. Ultimately, *in situ* XRD fosters accelerated material development by minimizing iterative *ex situ* analyses, and providing real-time data on precipitate volume fraction and phase formation. At the same time, TEM processing can be sluggish, also presenting a static perspective that limits kinetic insights, whereas *in situ* XRD bridges microstructural evolution to macroscopic performance, reducing experimental testing.

The present work aimed to study precipitation evolution and the influence of heat rate on commercial Scalmalloy® using *in situ* XRD and supported by TEM analysis. Heat treatments at 400, 375, and 275 °C for different soaking times were performed coupled with an *in-situ* HEXRD beamline (P07) in the German Electron Synchrotron (DESY). The experiments reveal the effects of nucleation and growth of precipitates throughout different thermal cycles, with heat treatment at 275 °C presenting a smooth increase of hardness with fine precipitate formation, while aging at 400 °C rapidly coarsens the formed intermetallics.

2. Experimental procedure

Commercial AlSc powder from AP Works was processed by PBF-LB, using a EOSINT M280 equipment from EOS GmbH, installed at INCT-BIOFABRIS. The process parameters used were those optimized for AlSiMg alloys as defined by the manufacturer and were not provided to the users [13]. However, the typical processing range of Scalmalloy by PBF is between 350 and 400 W, scanning speed of 1000 to 1500 mm/s (or lower power, as 240 W, combined with lower scanning speed, as 500 mm/s for aluminum material [11]), with hatch spacing of 90 to 120 μm and layer thickness generally from 30 to 60 μm [23]. The chemical composition of the powder was measured by inductively coupled plasma atomic emission spectrometry (ICP-OES) and given in Table 1, along with the compositional limits provided by AP Works. The powder morphology is shown in scanning electron microscopy in Fig. 1. The metallic powder utilized in this study was spherical, with a mean particle size of 45 μm. This spherical morphology, combined with a uniform particle size distribution, is highly desirable for PBF processes. Spherical particles promote efficient packing within the powder bed, leading to improved layer density, reduced porosity, and enhanced mechanical properties of the final product. Furthermore, a consistent particle size distribution minimizes the potential for voids and defects within the printed parts, ensuring optimal build quality and part integrity.

Thermodynamic equilibrium simulations were conducted using Thermo-Calc® software and the TCAL8 database to guide the phase formation near room temperature, phase fraction, and composition. This tool was used mainly to estimate the precipitates found in the microstructure. PRISMA module was used to calculated the AlSc precipitate mean size, density and nucleation rate for 275 °C/2 h, 325 °C/2 h and 400 °C/5 min as experimentally performed, also using TCAL8 database.

Microstructural characterization was performed using light optical microscopy (LOM – model Leica DMi8), scanning electron microscopy (SEM, Thermo Fisher Quanta 650 FEG), and transmission electron microscopy (TEM) associated with energy dispersive X-ray spectroscopy (EDS) (JEOL JEM-2100F and ThermoFisher CM-200 T microscopes). For TEM analysis, 200 μm thick specimens were extracted from the sample surfaces using a diamond saw (Buehler ISOMET 4000) and prepared via conventional "plan view" methodology. Final precision ion polishing (PIPS) with argon to achieve electron transparency (≤100 nm thickness) was conducted.

Hardness measurements were performed in bulk samples using a Buehler Vickers 2100 equipment, applying a load of 0.5 kgf for 10 s, 5 measurements per condition. A progressive aging heat-treatment was performed to evaluate the hardness evolution, using temperatures of 275, 325 and 375 °C, during 10 min, 1, 4, 10, 16, 24 and 36 h.

In-situ HEXRD measurements were performed at the High Energy Materials Science (HEMS) beamline P07 at PETRA III in the German Electron Synchrotron (DESY). The beam energy used was 81.1 keV, corresponding to a wavelength of 0.1423 Å. X-ray diffractions were obtained in transmission mode, using a fast 2D Perkin Elmer detector to capture Debye-Scherrer diffraction rings. Combined heat treatment was performed using a DIL-805 Bähr dilatometer. The data obtained were post-processed using Fit2D and HighScore plus software to get full width at half maximum (FWHM) and lattice parameter variation during the heat treatment. Thermal cycles are described in Table 2.

3. Results

3.1. Thermo-Calc simulation

Concerning the aged conditions, Scalmalloy® presents a few different precipitate phases, which are very small. This can lead to the non-identification of the phase in TEM and sometimes the failure to find it. Thus, Thermo-Calc® was a useful tool in predicting which phases to expect, as the literature reports few intermetallic formations such as Al_3Sc, $Al_{12}Mg_{17}$, and Al_6Mn [17,24,25]. Thermo-Calc simulations are depicted in Fig. 2. The literature widely reports the formation of Al_3Sc [24,25], which was confirmed by Thermo-Calc simulations as Al_3X. The Al_3Sc is presented as $Al_3(Sc,Zr)$ by chemical composition in the resulting simulations, with an equilibrium proportion of $Al_3Sc_{0.84}Zr_{0.17}$, commonly addressed as Al_3Sc. The prediction of a lower temperature for precipitation, below 200 °C, is unlikely to occur due to low diffusivity, even if it is predicted in equilibrium conditions. These were AlMg and $Al_{12}Mn$. The Al_6Mn precipitate would present an aluminum enrichment

Table 1
Chemical composition of the Scalmalloy® alloy and its theoretical range.

Wt%	Mg	Sc	Zr	Mn	Si	Fe	Zn	Cu	Ti	O	V
Min.	4.00	0.60	0.20	0.30	0.00	0.00	0.00	0.00	0.00	0.00	0.00
Max.	4.90	0.80	0.50	0.80	0.40	0.40	0.25	0.10	0.15	0.05	0.05
Powder wt%	4.230	0.66	0.26	0.6	0.51	0.099	0.005	0.00	0.02	0.03	0.01

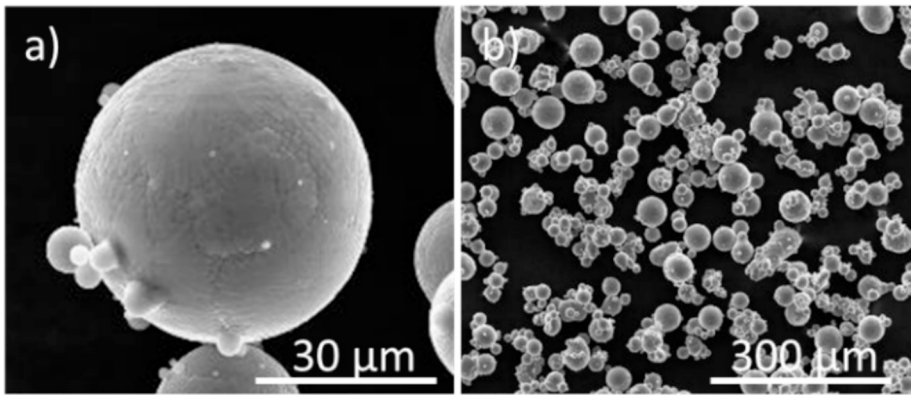

Fig. 1. Scalmalloy® spherical powder for PBF-LB process.

Table 2
Heat-treatment description with HEXRD experiment.

Sample	Heating rate	Isothermal	Cooling rate
AS1	0.167 °C/s	400 °C/5 min	5 °C/s
AS3	0.833 °C/s	400 °C/5 min	5 °C/s
AS4	50 °C/s	275 °C/2 h	5 °C/s
AS6	50 °C/s	325 °C/2 h	5 °C/s

being transformed to $Al_{12}Mn$. However, literature has only reported Al_6Mn until now [24], and no AlMg has been reported. Furthermore, Mg_2Si was found only in alloys with higher Mg content [26]. Therefore, it is expected to find an FCC matrix with precipitates of $Al_3(Sc,Zr)$ and Al_6Mn.

3.2. Microstructural characterization in the as-built condition

Fig. 3 reveals the LOM images from the studied Scalmalloy® fabricated by PBF-LB. The solidification profile has a semicircular shape, in the build direction, characteristic of PBF-LB processes, as depicted in Fig. 3a. It is possible to verify that the width of the melt pools was approximately 200 µm, while the depth was approximately 90 µm (Fig. 3b). Koutny et al. [23], obtained similar results when processing an AlSc alloy with scandium contents close to 1.1 wt%. Considering that the laser scan passes perpendicularly to this face, these semicircles suggest the paths through which the laser beam melts the metal powder. The semicircular geometry of the molten pools can be attributed to the characteristics of the laser, especially the Gaussian profile of the laser beam energy distribution and the energy density used during the energy processing.

Microscopy using polarized light, shown in Fig. 3b, reveals the structure of the grains inside the melt pools. Two very distinct microstructure regions are formed: an area of very fine grains, with sizes between 150 nm and 1 µm, close to the contours of the melt pools. Another region inside the melt pools is characterized by the presence of columnar grains with sizes between 2 and 15 µm, which grew perpendicular to the molten pool in the opposite direction of heat extraction, as observed in Fig. 3b.

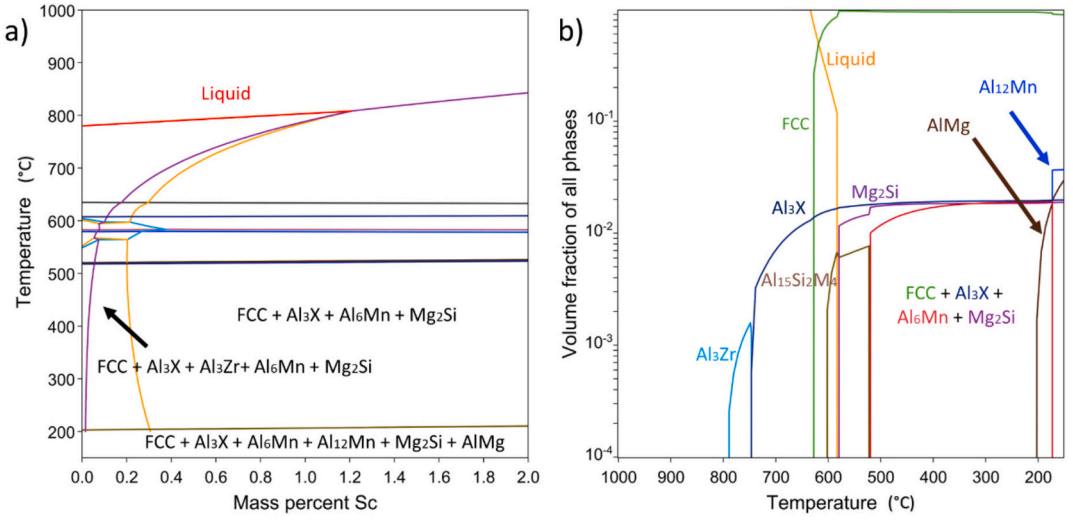

Fig. 2. Thermo-Calc® simulations are shown in a) the isopleth of Scalmalloy® using Al, Sc, Zr, Mg, and b) Mn components.

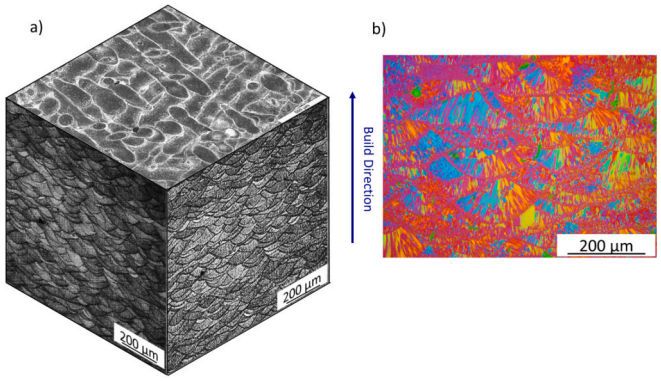

Fig. 3. LOM images showing the microstructure of the Scalmalloy® samples. In a) schematic cube showing all three planes of PBF-LB fabrication; in b) polarized LOM from the transverse plane.

3.3. Microstructural characterization in the aged conditions

The micro-sized region was analyzed to identify precipitation formation with the help of TEM investigation. Fig. 4 shows the TEM images of Scalmalloy® in the heat-treated AS3 condition. From the TEM results, it can be observed that nano-sized nanometric precipitates were formed in the microstructure. The SAED pattern reveals weak diffraction, confirming the formation of Al_3Sc, of the $L1_2$ type.

A heterogeneous distribution of the precipitates was observed in the micro-sized region and also embedded in a few areas, as depicted in Fig. 4, but mainly, the nucleation seemed to occur near the grain boundary and across the microstructure.

Fig. 5 shows the evolution of the microstructure regarding Al_6Mn precipitation when aging was performed, from 400 °C/5 min to 325 °C/2 h (Fig. 5a-b). Al_6Mn is confirmed by EDS, shown in Fig. 5c. It can be observed that the slow heating rate of 0.833 °C/s caused gradual and fine precipitation of Al_6Mn when aging was achieved (Fig. 5a). Many fine and nanometric nuclei were formed before reaching the target temperature of 400 °C, and as a gradual temperature increase occurred, coarsening started to happen. In contrast, sample AS6 (325 °C/2 h) was subjected to a heating rate of 50 °C/s, not having enough diffusional time to nucleate finely. This led to less dispersed Al_6Mn with coarser precipitates. This result reveals a precipitation start under 325 °C, and that holding heating treatment at 400 °C for 5 min is not enough to strongly dissolve the fine Al_6Mn, causing coarsening.

3.4. In-situ HEXRD analysis

Fig. 6 depicts the *in-situ* HEXRD from the aging of samples as-built, AS1, AS3, AS4, and AS6. The diffraction pattern shown is the last acquisition of HEXRD in the DESY P07 line. Spectra ranged from 2θ angles between 3.2° and 8° for all aged conditions. It can be observed that the diffraction peaks slightly decreased in width, probably due to an increase in crystallite size after heat treatment [19]. Regarding precipitate formation, all conditions presented precipitation of what was identified as Mg_2Si, having {220} and {311} peaks at 3.63° and 4.26°, also reported in the literature for Al-Mg-Si alloys [27]. The as-built condition seemed to present a small diffraction of the Al_6Mn phase. From increasing aging heat treatment time from 400 °C/5 min to 325 °C/2 h (AS1/3 to AS6), an increase of Al_6Mn diffraction peak was

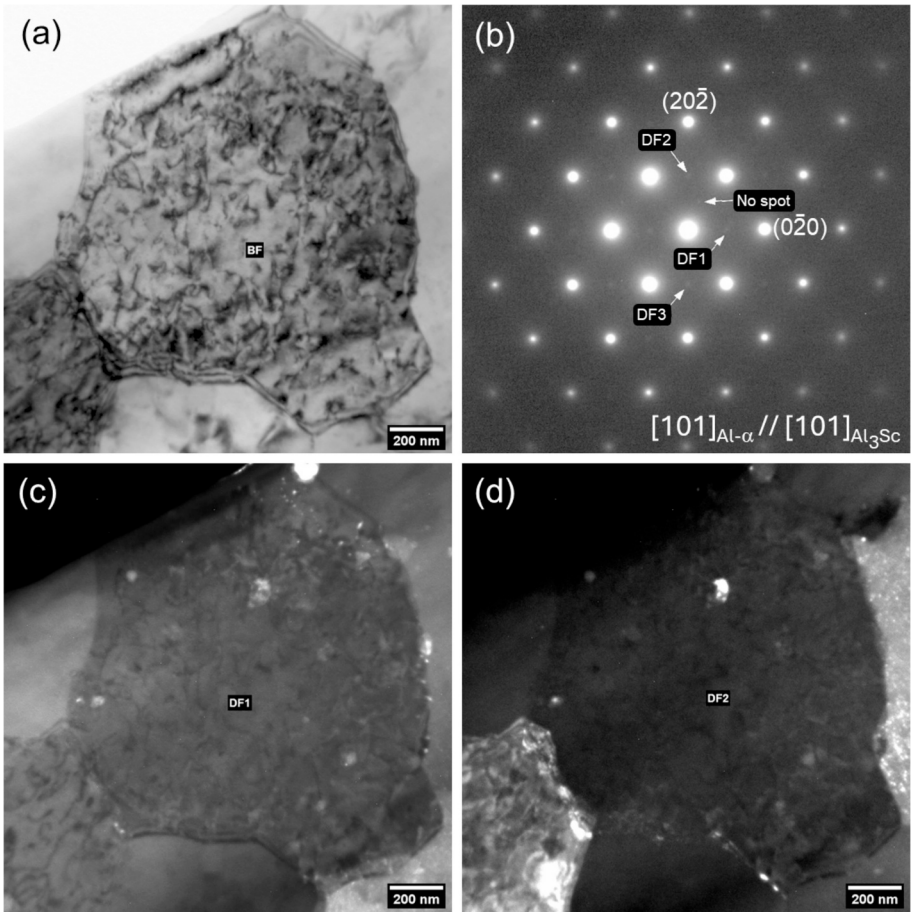

Fig. 4. TEM images of PBF-LB of the AS3 (Aged at 400 °C/5 min, the heating rate of 0.833 °C/s): (a) Bright-field image of material; (b) SAED pattern; (c-d) dark field images from specific SAED showing precipitates.

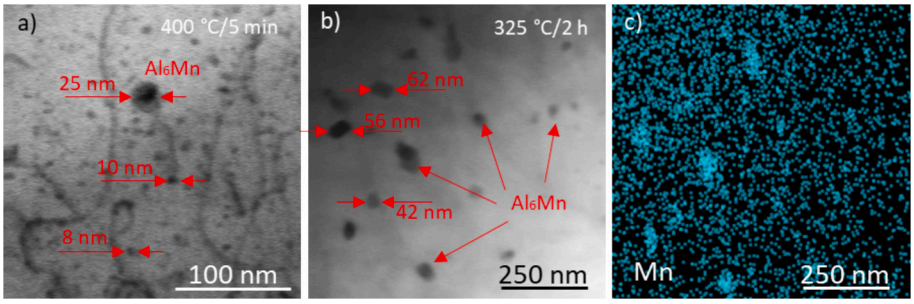

Fig. 5. TEM and EDS analysis of coarsening of Al_6Mn precipitate from aging 400 °C/5 min (AS3) and 325 °C/2 h (AS6). In a) STEM image of AS3 condition, b) AS6 condition, and c) Mn in AS6 condition.

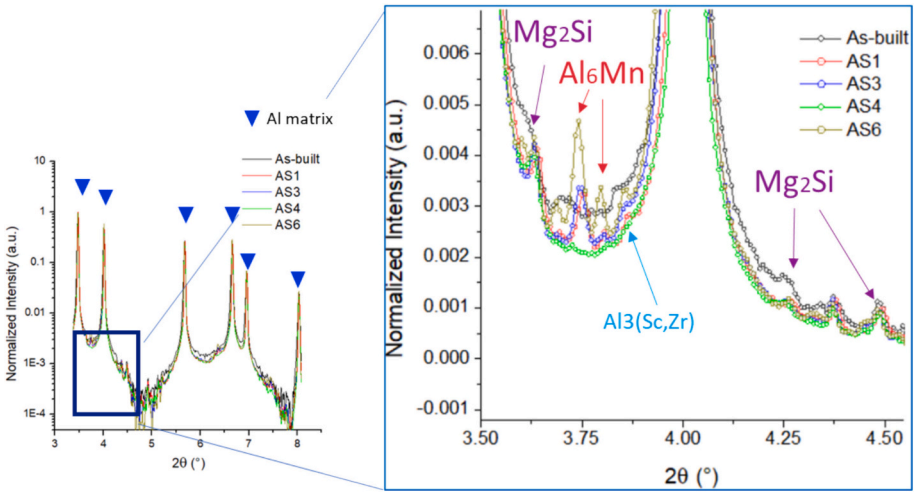

Fig. 6. HEXRD pattern from as-built, AS1 (400 °C/5 min-0.167 °C/s), AS3 (400 °C/5 min-0.833 °C/s), AS4 (275 °C/2 h-50 °C/s) and AS6 (325 °C/2 h-50 °C/s) samples after heat treatment. XRD pattern reveals the formation of peaks indexed as precipitates, specifically Mg_2Si, Al_6Mn, and $Al_3(Sc,Zr)$ phases.

observed, which is in agreement with the TEM findings of the AS6, where coarse Al_6Mn was found, and EDS confirmed Mn concentration (Fig. 5c). Also, AS4 did not present diffraction of Al_6Mn, suggesting that Al_6Mn starts to precipitate above 275 °C and under 325 °C as stated above.

$Al_3(Sc,Zr)$ precipitate was found to be formed during PBF-LB. This precipitate presents XRD peaks that coincide with the aluminum matrix due to the same FCC crystal arrangement and similar lattice values (Al 4.094 Å and $Al_3(Sc,Zr)$ 4.103 Å), making it difficult to index. However, literature widely reports its formation during the AM process [4,25,26]. Observing Fig. 7, it can be seen that there is a convolution of $Al_3(Sc,Zr)$ peaks to the Al peaks as expected by theoretical diffraction shown in Fig. 7a, confirming the formation of Al3(Sc,Zr) in the as-built condition, as well as in heat-treated conditions. The experimental peak in.

Fig. 7b at 3.86° can be attributed to the $Al_3(Sc,Zr)$ {111} plane. It can be observed that the $Al_3(Sc,Zr)$ {111} peak starts to separate from the Al, which corresponds to growth, a more defined composition, and a crystal arrangement. The rapid cooling rates inherent to the PBF-LB process retain a significant fraction of Sc and Zr in supersaturated solid solution. Although initial precipitation already occurred in PBF-LB processing, this enables subsequent precipitation of finely dispersed, coherent $Al_3(Sc,Zr)$ particles during post-processing heat treatment as reported by Spierings [28].

The evolution of the *in-situ* HEXRD pattern can be observed as heat treatment occurs for samples AS3 and AS6, as shown in Fig. 8, where the numbers in legend represent the N^{th} diffraction pattern (AS3 had a total of 653 diffractions and AS6 a total of 1713 diffractions). This result reveals an important characteristic that significant precipitation starts to appear above 300 °C, as observed in the slow heating treatment of condition AS3 in Fig. 8a. From 192 °C to 279 °C, no perceptible change in the XRD is observed, suggesting no precipitation reaction. However, an XRD profile change is noticed from 279 °C to 400 °C, specifically in precipitate diffraction. At sample AS6, precipitation is observed in diffraction number 50 already due to the fast-heating rate, reaching the 325 °C target temperature in less than 1 min. This result showed that the heating rate seemed to be irrelevant to precipitation, contrasting with time at high temperature (>300 °C), which appeared to have a major impact, resulting in increased diffracted peaks observed in Fig. 8b when compared to Fig. 8a in the last diffraction profile (*i.e.*, AS3–500, AS6–1500).

3.5. Hardness

Hardness was assessed by microscale measurements, applying a load of 0.5 kgf for 10 s. The indentation is small enough to avoid microstructural features, such as the indenting region of large grains, as depicted in Fig. 3. Therefore, 5 measurements were made around a mean spot, and 3 mean spots were selected to avoid microstructural bias. The results are plotted in Fig. 9 and are coherent to an alloy susceptible to intermetallic precipitation, presenting a peak hardness over time, followed by a decrease in hardness.

The as-built condition presented the lowest hardness, resulting in 100 HV. Aging led to a hardness increase, and as expected, the highest temperature of 375 °C reached the hardness peak earlier, in 1 h. In comparison, the lowest aging temperature of 275 °C presented a hardness increase up to 24 h of aging. The maximum hardness mean value was 174 HV, corresponding to the 275 °C/24 h condition. The maximum achieved hardness from the other aging temperatures was 167 HV and

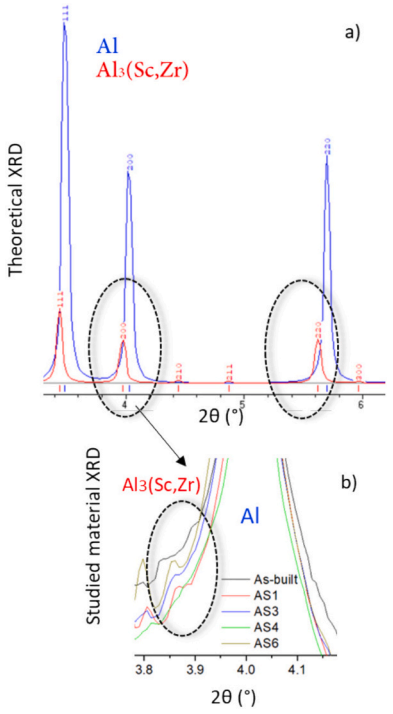

Fig. 7. The XRD pattern compares the a) theoretical reference material and the b) material studied below. The $Al_3(Sc,Zr)$ peaks are found on the left side of the Al peaks with a very close 2θ diffraction value, making it more difficult to identify in the XRD. The obtained XRD shows traces of the $Al_3(Sc,Zr)$ presence.

164 HV for 325 °C/10 h and 375 °C/1 h, respectively. Thus, it can be observed that the maximum hardness achieved from each heat-treatment temperature was not far from each other's value, giving a difference of less than 6%, but with a heat-treating time difference of 23 h, considering 275 and 375 °C peak-aged conditions.

4. Discussion

4.1. Microstructure and precipitation

This paper reviewed the precipitate formation during aging using TEM and *in-situ* HEXRD to identify its components, morphology, and distribution in the microstructure of the Scalmalloy fabricated by PBF-LB. Initial Thermo-Calc® simulations in Fig. 2 predicted $Al_3(Sc,Zr)$, Al_6Mn, and $Al_{12}Mg_{17}$ intermetallic formation in a temperature range of 200 °C up to 500 °C. Thus, the studied aging cycles were expected to give rise to some or all these constituents, as widely reported in the literature [9,17,23,25,26]. Due to the thermal cycling of layer-by-layer construction, the microstructure comprised of columnar and fine-grain regions produced from the PBF-LB process. This induces very fine, sometimes addressed as submicron-sized region, *i.e.*, nanometric grain formation, always appearing near the melt pool track [17,26,29]. In addition, the PBF-LB as-built condition presented precipitate formation, which was also reported [17,25,26]. Due to the PBF-LB process, the heat dissipated to the lower layers leads to the precipitation of small $Al_3(Sc,Zr)$ agglomerates since this layer probably reached temperatures within the precipitation region. The HEXRD data presented was able to identify and confirm the precipitation of $Al_3(Sc,Zr)$ after PBF-LB process, and evolution during posterior heat-treatments, conferring a significant increase in mechanical strength, as confirmed in Fig. 9.

Previous works [16,18,28] explored the effect of heat treatments on the microstructure of samples processed *via* PBF-LB, using typical temperatures of 300, 325 and 375 °C for heat treatments. All observed little or no change in the average grain size, which is advantageous due to many fine grains without preferential orientation. Furthermore, the gains in mechanical properties evidence that the strengthening mechanism is related to the precipitation of $Al_3(Sc,Zr)$ particles. Spierings et al. [28] found that the numerical density of $Al_3(Sc,Zr)$ particles increased by 3 to 10 times when comparing the as-built condition with heat-treated conditions. During aging, the growth of $Al_3(Sc,Zr)$ particles occurs, which would lead to overaging when the treatment is performed outside the optimal time and temperature conditions [16,18]. It is believed that fast and very stable precipitation of $Al_3(Sc,Zr)$ occurs already during PBF-LB due to the similarity of crystal lattice size and arrangement (FCC) [25]. Thus, $Al_3(Sc,Zr)$ would be rapidly precipitated during thermal cycling of the AM [9].

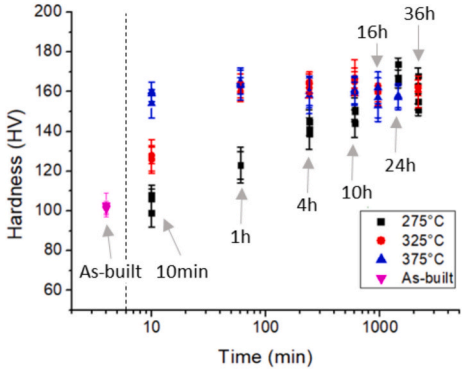

Fig. 9. Hardness assessment of the Scalmalloy® according to several aging treatments applied.

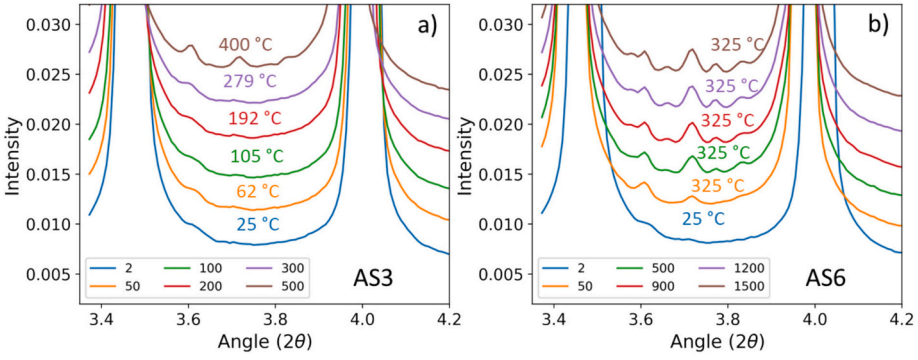

Fig. 8. *In-situ* HEXRD pattern evolution shows the growth of the precipitate phase during the aging of Scalmalloy. Numbers in legend represent the N^{th} diffraction pattern in a) AS3 heat-treatment condition; in b) AS6 heat-treatment condition.

4.2. HEXRD analysis on heating rate effect

As far as is known, no result comparing the heating rate effect has been reported yet regarding precipitation in Scalmalloy. The present study reveals more details about $Al_3(Sc,Zr)$ further nucleation and growth upon posterior heat treatment based on HEXRD from samples heated at 0.167 and 0.833 °C/s (respectively AS1 and AS3 conditions), as shown in Fig. 10.

The identification of precipitation is perceived as an increase in the lattice, which was graphically depicted by the derivative for a better observation of the change. Fig. 10 shows a steady lattice derivative curve in the beginning, followed by a positive change in the inclination, which defines the beginning of precipitation due to $Al_3(Sc,Zr)$ intermetallic, with a larger lattice parameter than the Al matrix. After reaching a peak, it decreases due to deceleration of the nucleation process and relaxation phenomena involved in the atoms' accommodation in the structure upon new phase forming [30].

The application of two different heating rates opened a path to observe by *in-situ* HEXRD the differences in precipitation among them. It can be seen that $Al_3(Sc,Zr)$ starts to precipitate near 212 °C when heated at the rate of 0.167 °C/s, while growth and coarsening had their onset over 300 °C. For a higher heating rate of 0.833 °C/s, these temperatures were found to be superior, presenting onset precipitation of $Al_3(Sc,Zr)$ at 246 °C, and growth over 335 °C. These temperatures are marked with light gray lines and were found using the first derivative from the {111} lattice parameter combined with changes in the FWHM curve. Steels also present anticipation of phase transformation when subjected to slower heating rates, contrasting to overheating when subjected to higher heating rates [30–32]. Furthermore, a decrease in FWHM is expected due to crystal relaxation at the first stages of precipitation from a supersaturated solid solution [22].

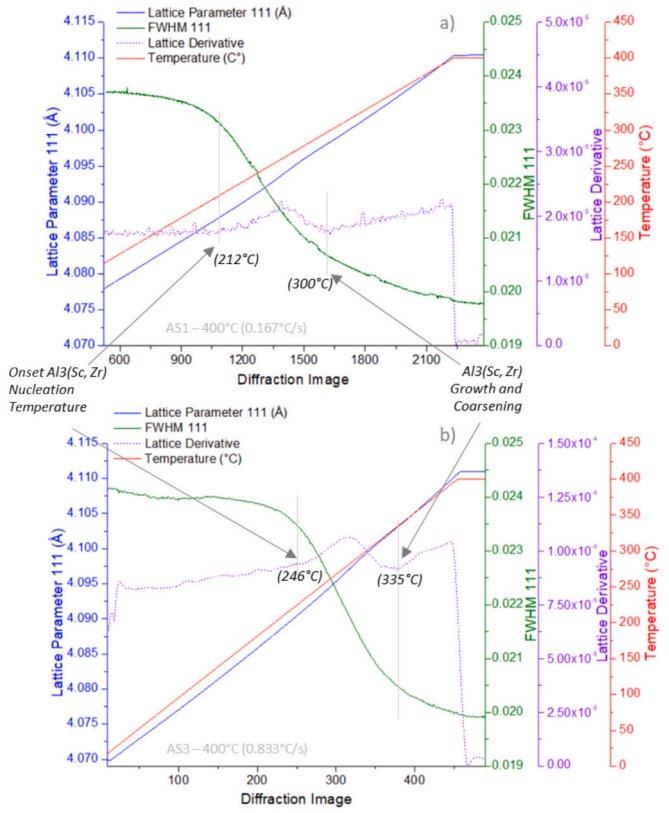

Fig. 10. *In-situ* HEXRD analysis showing lattice parameter, its derivative, FWHM, and temperature. In a) AS1 and in b) AS3 samples (target temperature of 400 °C with heating rates of 0.167 and 0.833 °C/s, respectively).

4.3. HEXRD combined with dilatometry analysis for precipitation evolution

HEXRD combined with dilatometric analysis provided richer insights. The HEXRD and dilatometric data are presented in Fig. 11, showing lattice parameter and dilation values, with their respective derivative values. Five distinct phenomena can be observed:

i) *Onset of $Al_3(Sc,Zr)$ Precipitation (212 °C)*: $Al_3(Sc,Zr)$ nucleation started near 212 °C as depicted. The identification as $Al_3(Sc,Zr)$ intermetallic is possible due to a slight increase in the lattice derivative of the $Al_{\{111\}}$ parameter, representing a larger expansion rate than heating dilation, indicating the formation of a new phase. When $Al_3(Sc,Zr)$ precipitates, the {111} peak forms near the $Al_{\{111\}}$, dislocating the peak center to lower diffraction angles, increasing the lattice value in the XRD acquisition. Although $Al_3(Sc,Zr)$ precipitate yields a larger lattice than Al (which means a lower density), the early stage of precipitation is marked by a decrease in dilation. This is related to a higher magnitude of elastic relaxation due to the decrease of the supersaturated solid solution in the Al matrix by $Al_3(Sc,Zr)$ formation rather than the increase of volume by the $Al_3(Sc,Zr)$ itself.

ii) *Precipitation peak rate (~270 °C)*: lattice {111} derivative from 1200 and 1500 diffraction images shows a peak form, with an increase followed by a decrease. This is translated to an acceleration of precipitation (nucleation+growth), reaching a peak, and then a deceleration in the precipitation rate, shown as a decrease of lattice derivative.

iii) *Precipitation rate deceleration (near 300 °C)*: this stage is characterized by the decrease of lattice derivative and dilation, reaching a valley with posterior increase of lattice and dilation derivative.

iv) *Lattice and dilation derivatives expansion (300–379 °C)*: this stage was characterized by the restart of lattice derivative and dilation derivative increase. The increase in lattice derivative would indicate a continuous increase in the total volume of the $Al_3(Sc,Zr)$ phase. The dilation derivative parameter starts to increase after 300 °C, indicating a volume increase of $Al_3(Sc,Zr)$. The

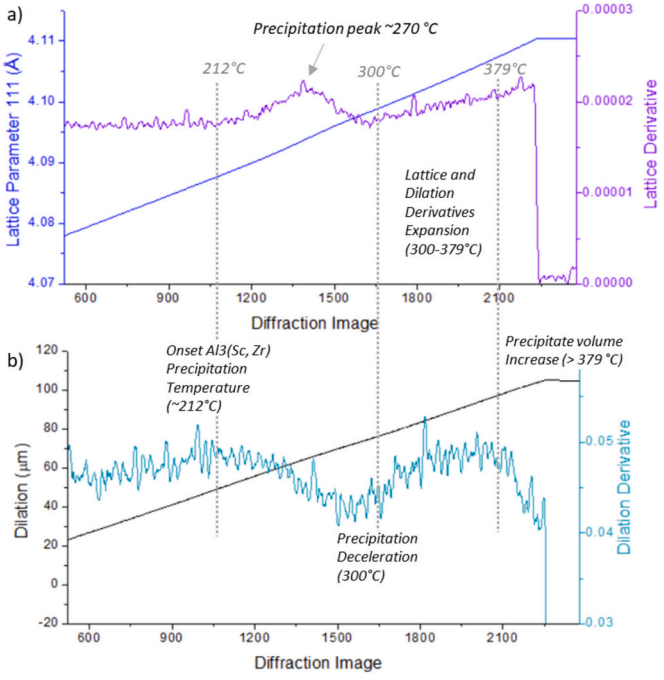

Fig. 11. AS1 *in-situ* a) HEXRD and b) dilatometric results during 0.167 °C/s heating up to 400 °C.

behavior of lattice increase (ii), followed by decrease (iii) and subsequent increase (iv) suggests that in the latter range, from 300 °C up to 379 °C (temperature range where dilation derivative starts to increase), coarsening of precipitates prevails above nucleation. In contrast, the total volume of $Al_3(Sc,Zr)$ slightly increases. The lattice increase could also indicate a switch of precipitation mechanisms: higher dissolution of very small precipitates, with growth of $Al_3(Sc,Zr)$, instead of higher nucleation rates. The early stage of nucleation results in precipitates with a very similar structure to the matrix, usually following a precipitation sequence: supersaturated solid solution (SSSS) → solute clusters (SC) → Guinier-Preston I (GPI)/Guinier-Preston II (GPII) zones → equilibrium condition (EC) [33]. Growth of $Al_3(Sc,Zr)$ precipitates would cause a gradual structure transition mentioned above (SSSS→SC → GPI/GPII→EC), resulting in a gradual increase of crystal lattice, and thus a better identification of HEXRD peaks due to $Al_3(Sc,Zr)$ 2θ separation from the Al matrix. As $Al_3(Sc,Zr)$ and Al present FCC structure and similar lattice value, the convoluted peak is a accounted as a single peak during data analysis, generating a mean lattice value of the two phases. As heat-treatments continue, temperature rises gradually, increasing $Al_3(Sc,Zr)$ total volume by coarsening of particles. In addition, the higher temperature leads to peak narrowing of the Al matrix due to stress relaxation, resulting in a better distinction between Al and $Al_3(Sc,Zr)$ peaks in the diffraction pattern [19], and contributing to the observation of lattice increase (illustrated in Fig. 12c). Furthermore, PRISMA® simulation showed that the maximum nucleation rate near 325 °C is sustained for less than 1 min (Fig. 13c), suggesting that beyond this temperature, there is an increase of coarsening rate at the expense of nucleation rate. As it is a continuous heating experiment, transient behavior is expected, and it is possible that a major nucleation phenomenon gave place to growth/coarsening during the heating stage, with further volume increase as the temperature rose.

v) *Precipitate volume increase (>379 °C)*: the lattice derivative continues to increase with combined decrease in dilation derivative, pointing out an increase of $Al_3(Sc,Zr)$ phase volume or other intermetallic precipitation.

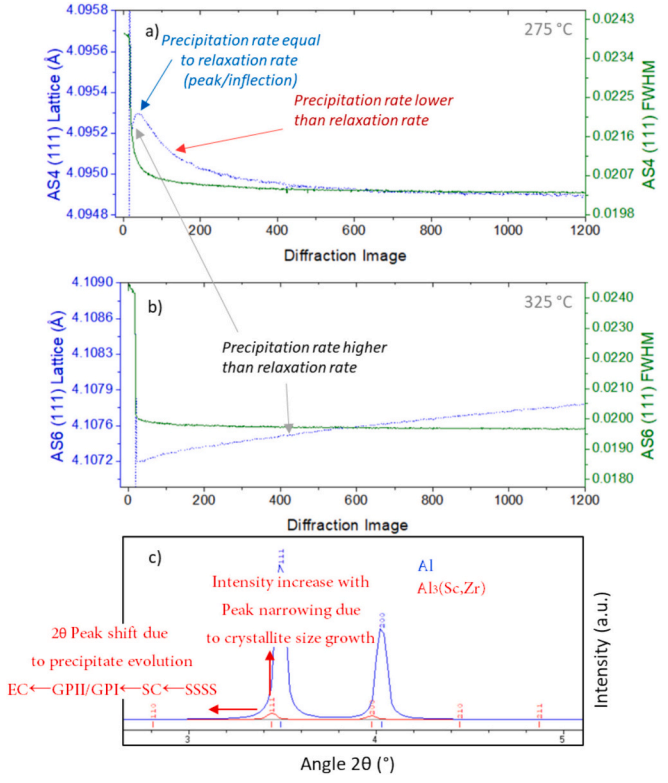

Fig. 12. Lattice with FWHM plot of a) AS4 (275 °C – 50 °C/s) and b) AS6 conditions (325 °C – 50 °C/s). In c) schematic illustration of the displacement of the diffraction peak due to $Al_3(Sc,Zr)$ precipitation and the impact of intensity increase and peak narrowing due to crystallite growth/coarsening.

4.4. HEXRD analysis for target temperature effect

FWHM value displays another important characteristic. An ideal crystal, large and defect-free, would produce extremely narrow diffraction peaks, almost like vertical lines (FWHM tending to zero). However, the peaks always have some width due to instrumental factors and, more importantly, the characteristics of the material [19]. Basically, the broadening of XRD peaks, *i.e.*, a larger FWHM, is directly related to the crystallite size and microdeformations in the crystal lattice, or crystal defects [19]. As observed in Fig. 12, FWHM for both conditions, AS4 and AS6, decreases during the whole heat-treatment, concluding that there is a process of recovery from internal stress originated during PBF-LB processing, which is likely to be based on the rearrangement of dislocations, as well as the annihilation of dislocations.

4.5. Thermodynamic precipitation simulations: PRISMA

Al_6Mn was found during aging and posterior coarsening (Fig. 5 and Fig. 6) by TEM-EDS analysis. For $Al_3(Sc,Zr)$, coarsening was found during *in-situ* HEXRD, aided by PRISMA® precipitation calculation as shown in Fig. 13. Thermodynamic simulations were used to calculate precipitate mean size (in length), number density distribution, and nucleation rate for 275, 325, and 400 °C. It can be observed that for the temperature of 275 °C, longer periods at maximum nucleation rate are provided, and as expected, increasing temperature causes a decrease in the maximum nucleation rate plateau. Identifying precipitates by XRD analysis is sometimes difficult due to the many peak diffractions. Specifically, the $Al_3(Sc,Zr)$ presents a coherent precipitation with the matrix due to the same FCC crystal arrangement. Thus, the XRD peaks of the $Al_3(Sc,Zr)$ may be hidden in a convoluted peak, as in the present case in Fig. 6, and as reported [25]. Hardness peak of 143 HV was reached 10 h after the start of treatment; times longer than this caused overaging of the samples [2]. Schmidtke et al. [34] and Koutny et al. [23] reported a maximum hardness of 177 HV after heat treatment at 325 °C for 4 h, similar to the present case. PRISMA® results bring useful information about precipitate size as well, showing a very slow growth of precipitate upon 275 °C aging. This may be the reason why it was not possible to find precipitates in TEM for the 275 °C condition. Contrastingly, through TEM analysis, precipitates were found on 325 and 400 °C heat-treated samples, as shown in Figs. 4 and 5. Another result that reinforces the difficulty of finding precipitates on a 275 °C/2 h sample by image analysis, such as TEM, is the lattice and dilation derivative combined with hardness evolution, showing precipitation starts near 250 °C (Fig. 10 and Fig. 11), and a poor hardness evolution of only 15 HV after 1 h at 275 °C (Fig. 9).

The nucleation rate at 275 °C was simulated as the lowest among the target temperatures studied, as expected for a lower temperature. With a precipitation onset temperature of 250 °C, a low phase formation rate was expected. Crystallographic lattice behavior for 275 and 325 °C was distinct due to different rates of nucleation and relaxation, as observed in Fig. 12. For an aging at 275 °C, the onset of precipitation is characterized by fast nucleation and an increasing lattice value. The increase in lattice is due to two main factors: a) volumetric change in the system due to phase precipitation, and b) dislocation of the peak position to lower 2θ values due to precipitate evolution, illustrated in Fig. 12c.

a) *Volumetric change:* The transformation may involve an atomic rearrangement that, despite the theoretical difference in density of the

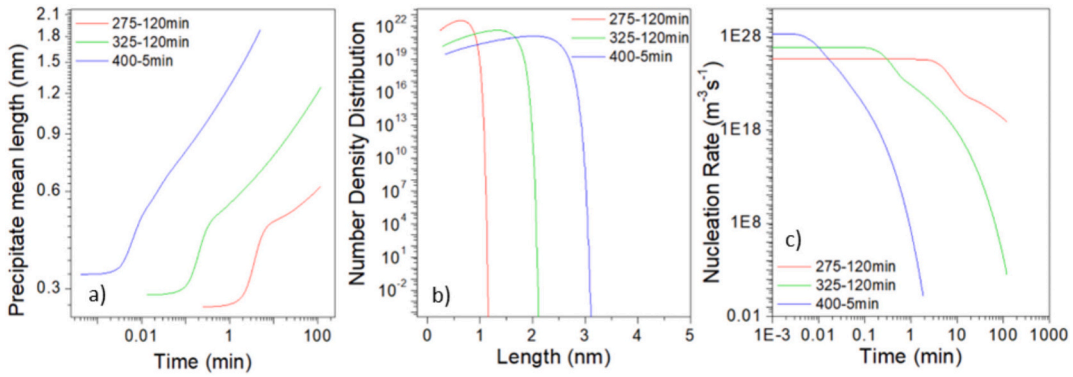

Fig. 13. PRISMA® simulation regarding Al_3Sc precipitation on Al-Sc alloy.

isolated phases, results in an accommodation of stresses in the matrix lattice that minimizes the net dimensional change. $Al_3(Sc,Zr)$ presents a density slightly lower than the Al matrix, causing misfit with a local compression upon $Al_3(Sc,Zr)$ formation, deforming the Al lattice in order to accommodate it.

b) *Peak displacement:* as the material is heated, precipitation continues, causing nucleation and/or growth/coarsening of the intermetallics. The intermetallics will go through the mentioned sequence of SSSS→SC → GPI/GPII→ EC [33], resulting in a gradual increase in the crystal lattice. As $Al_3(Sc,Zr)$ and Al {111} peaks are convoluted, a mean decreasing peak position was found, thus a mean increasing lattice parameter as $Al_3(Sc,Zr)$ converges to its equilibrium structure condition. A smooth lattice decrease is observed for the AS4 (275 °C) sample in Fig. 12a because the temperature is not high enough to cause progression of the $Al_3(Sc,Zr)$ towards SSSS→SC → GPI/GPII→ EC. After a short period, a peak in lattice size is achieved, followed by continuous decrease, suggesting a lower nucleation/growth rate than structure relaxation (Fig. 12a). Contrasting, aging at 325 °C seems to continuously cause precipitation, maintaining whether nucleation and growth rate above lattice relaxation rate, consequently depicting a continuous increase of lattice absolute value as shown in Fig. 12b.

4.6. Impact of precipitation on the microstructure

As reported, the HEXRD provided meaningful insights about $Al_3(Sc,Zr)$ kinetics and evolution during *in-situ* heat treatment. The total volume fraction was found to increase during all heat treatments, as observed in Fig. 12, mainly at 325 °C, where the lattice is constantly increasing, meaning the formation of Al-Sc intermetallic. The precipitates are expected to grow above 300 °C, as shown by the combined analysis of lattice and dilation derivative in Fig. 11, described in stage (iv). This is in accordance with PRISMA simulation in Fig. 13, where a high nucleation rate is observed during the 2 h of heat-treatment at 275 °C, contrasting with a fast decrease of nucleation rate when heat-treated at 325 °C. This is followed in practice by the hardness evolution in Fig. 9, where the peak-age condition is reached after 1 h at 375 °C. Furthermore, it is expected to see a greater dispersion of precipitates when higher temperatures are applied, as observed in Fig. 13 by the precipitate mean length and number density distribution. As particle size increases, the density distribution decreases. The opposite is also true.

For aging at 325 and 275 °C, the peak-age condition seems to be after 10 h and 24 h, respectively. From the peak-age point, coherency would be lost if the precipitate had an atomic structure different from the matrix. However, $Al_3(Sc,Zr)$ presents the same structure with the lattice, maintaining coherency, only incurring overaging due to particle coarsening.

5. Conclusions

The results obtained in this work highlight the potential of the Scalmalloy® alloy processed *via* PBF-LB. The current work showed the influence of heat-treatment on PBFed samples and their precipitation behavior. The hardness observed both for the as-built condition and for the various aging processes performed agrees with the results found in the literature. The conclusions drawn are as follows:

- The *in-situ* analyses allowed us to verify the HEXRD behavior along with the aging for the studied Scalmalloy®. The indexing of $Al_3(Sc,Zr)$ intermetallic was facilitated using a high-energy X-ray diffraction (HEXRD). However, the same crystal arrangement (FCC) and similar lattice size (~4.1 Å) are found for Al and $Al_3(Sc,Zr)$, resulting in the convolution of the precipitate and matrix HEXRD peaks. As the heat treatment occurs, the lattice parameter undergoes a small increase, slightly separating the matrix from the $Al_3(Sc,Zr)$ precipitate with structure $L1_2$. During the aging heat treatment, there was an increase in the volume of the precipitates, observed by the diffraction and dilatometric analyses. HEXRD confirmed $Al_3(Sc,Zr)$, and Mg_2Si and Al_6Mn are possible phases formed. Al_6Mn was confirmed as observed in the EDS analysis with a high concentration of Mn.
- Onset of $Al_3(Sc,Zr)$ precipitation was found at 251 °C, with volume decrease due to its higher density, and lattice increase due to coherency with the matrix. Precipitation rate at 275 °C was lower than the recovery rate, enabling lattice value decrease during aging heat treatment. The opposite behavior was observed for 325 and 400 °C, having its lattice value increasing due to a higher nucleation/growth rate than recovery rate during aging treatment. In both cases, recovery took place, inferred by the continuous decrease in FWHM during aging.
- A peak hardness of 174 HV was obtained after the aging heat treatment, after 24 h of treatment at 275 °C. It is important to emphasize that the aging treatment at a temperature of 375 °C for 1 h resulted in a hardness close to the maximum (164 HV), indicating that it is possible to obtain hardness gains with short heat treatment times. Even for longer aging times, the aging treatment did not show an abrupt drop in hardness; it is possible to correlate this fact with little influence of the treatment time on the grain size of the alloy due to the high thermodynamic stability of the Al_3Sc precipitates.
- As-built condition presented early precipitation, mainly Mg_2Si, but also $Al_3(Sc,Zr)$ confirmed by HEXRD. Strength seemed to be mostly associated to $Al_3(Sc,Zr)$ and Al_6Mn precipitation, once as-built presented low hardness, and precipitation evolution of AS4 (275 °C/2 h) showed slow hardness evolution, as well as $Al_3(Sc,Zr)$ slow precipitation at 275 °C, and no precipitation of Al_6Mn after 2 h at 275 °C was found by HEXRD and TEM analysis.

CRediT authorship contribution statement

Fábio Faria Conde: Writing – original draft, Methodology, Investigation, Formal analysis. **André H.G. Gabriel:** Writing – review & editing, Formal analysis. **N. Schell:** Methodology, Investigation. **J.P. Oliveira:** Writing – review & editing. **Julian A. Avila:** Writing – review & editing, Methodology, Investigation, Formal analysis. **Eduardo B. da Fonseca:** Writing – review & editing, Formal analysis. **Éder S.N. Lopes:** Investigation, Resources, Supervision.

Declaration of competing interest

The authors declare that they have no known competing financial interests or personal relationships that could have appeared to influence the work reported in this paper.

Data availability

Data will be made available on request.

Acknowledgments

This project was financed by FAPESP (2008/57863-0) and CNPq (573661/2008-1 and 165208/2019-8), Coordenação de Aperfeiçoamento de Pessoal de Nível Superior – Brasil (CAPES) - Finance Code 001. This research used the facilities of the Brazilian Nanotechnology National Laboratory (LNNano), part of the Brazilian Centre for Research in Energy and Materials (CNPEM), a private non-profit organization under the supervision of the Brazilian Ministry for Science, Technology, and Innovations (MCTI). The authors acknowledge DESY (Hamburg, Germany), a member of the Helmholtz Association HGF, for providing experimental faclities. Beamtime was allocated for proposals I-20200371 EC. JPO acknowledges funding by national funds from FCT - Fundação para a Ciência e a Tecnologia, I.P., in the scope of the projects LA/P/0037/2020, UIDP/50025/2020, and UIDB/50025/2020 of the Associate Laboratory Institute of Nanostructures, Nanomodelling and Nanofabrication – i3N. J. Avila is a fellow from CNPq under grant 301561/2025-7.

References

[1] N.T. Aboulkhair, N.M. Everitt, I. Maskery, I. Ashcroft, C. Tuck, Selective laser melting of aluminum alloys, MRS Bull. 42 (2017) 311–319, https://doi.org/10.1557/mrs.2017.63.
[2] A.B. Spierings, K. Dawson, K. Kern, F. Palm, K. Wegener, SLM-processed Sc- and Zr-modified Al-Mg alloy: mechanical properties and microstructural effects of heat treatment, Mater. Sci. Eng. A 701 (2017) 264–273, https://doi.org/10.1016/j.msea.2017.06.089.
[3] A.B. Spierings, K. Dawson, M. Voegtlin, F. Palm, P.J. Uggowitzer, Microstructure and mechanical properties of as-processed scandium-modified aluminium using selective laser melting, CIRP Ann. Manuf. Technol. 65 (2016) 213–216, https://doi.org/10.1016/j.cirp.2016.04.057.
[4] M. Awd, J. Tenkamp, M. Hirtler, S. Siddique, M. Bambach, F. Walther, Comparison of microstructure and mechanical properties of Scalmalloy® produced by selective laser melting and laser metal deposition, Materials 11 (2017), https://doi.org/10.3390/ma11010017.
[5] R. Li, M. Wang, T. Yuan, B. Song, C. Chen, K. Zhou, P. Cao, Selective laser melting of a novel Sc and Zr modified Al-6.2 Mg alloy: processing, microstructure, and properties, Powder Technol. 319 (2017) 117–128, https://doi.org/10.1016/j.powtec.2017.06.050.
[6] A.F. Norman, P.B. Prangnell, R.S. Mcewen, The solidification behaviour of dilute aluminium scandium alloys, Acta Maerialia 46 (1998) 5715–5732.
[7] J. Röyset, Scandium in Aluminium Alloys Overview: Physical Metallurgy, Properties and Applications, Metallurgical Science and Technology, 2007.
[8] Z. Ahmad, The properties and application of scandium-reinforced aluminum, JOM 55 (2003) 35–39, https://doi.org/10.1007/s11837-003-0224-6.
[9] M. Wang, R. Li, T. Yuan, C. Chen, L. Zhou, H. Chen, M. Zhang, S. Xie, Microstructures and mechanical property of AlMgScZrMn - a comparison between selective laser melting, spark plasma sintering and cast, Mater. Sci. Eng. A 756 (2019) 354–364, https://doi.org/10.1016/j.msea.2019.04.060.
[10] A. Lama, D. John, T. Paul, A. Agarwal, Heat treatment induced precipitation and residual stress effects on tensile plasticity of cold-sprayed Scalmalloy deposits, J. Therm. Spray Technol. 34 (2025) 2211–2226, https://doi.org/10.1007/s11666-025-02030-3.
[11] K. Janus, A. Jarzębska, A. Wójcik, A. Garbacz-Klempka, J. Piekło, S. Terlicka, M. Piękoś, J.J. Sobczak, O. Krasa, Krawczyk, microstructure and mechanical properties of Scalmalloy® produced by selective laser melting in term of long-term applications, Arch. Civil Mech. Eng. 25 (2025), https://doi.org/10.1007/s43452-025-01242-2.
[12] N.W. Hughes, T.F. Flint, J.W. Fellowes, J.D. Robson, Effects of volumetric energy density on the microstructure of additively manufactured Scalmalloy, Mater. Charact. 230 (2025), https://doi.org/10.1016/j.matchar.2025.115701.
[13] L. Cabrera-Correa, L. González-Rovira, J. de Dios López-Castro, M. Castillo-Rodríguez, F.J. Botana, Effect of the heat treatment on the mechanical properties and microstructure of Scalmalloy® manufactured by selective laser melting (SLM) under certified conditions, Mater. Charact. 196 (2023), https://doi.org/10.1016/j.matchar.2022.112549.
[14] J. Lu, X. Lin, N. Kang, W. Huang, Characterizations of micro-nano structure and tensile properties of a Sc modified Al-Mn alloy fabricated by selective laser melting, Mater. Charact. 178 (2021), https://doi.org/10.1016/j.matchar.2021.111305.
[15] N. Jeyaprakash, C.H. Yang, M.S. Kumar, Influence of coherent intermetallic nano-precipitates on the nano-level mechanical and tribological properties of the laser-powder bed fused Scalmalloy, Mater. Charact. 193 (2022), https://doi.org/10.1016/j.matchar.2022.112269.
[16] R. Li, H. Chen, H. Zhu, M. Wang, C. Chen, T. Yuan, Effect of aging treatment on the microstructure and mechanical properties of Al-3.02Mg-0.2Sc-0.1Zr alloy printed by selective laser melting, Mater. Des. 168 (2019), https://doi.org/10.1016/j.matdes.2019.107668.
[17] C.N. Kuo, P.C. Peng, D.H. Liu, C.Y. Chao, Microstructure evolution and mechanical property response of 3d-printed scalmalloy with different heat-treatment times at 325°c, Metals (Basel) 11 (2021), https://doi.org/10.3390/met11040555.
[18] Q. Jia, P. Rometsch, P. Kürnsteiner, Q. Chao, A. Huang, M. Weyland, L. Bourgeois, X. Wu, Selective laser melting of a high strength Al-Mn-Sc alloy: alloy design and strengthening mechanisms, Acta Mater. 171 (2019) 108–118, https://doi.org/10.1016/j.actamat.2019.04.014.
[19] B. He, Two-Dimension X-Ray Diffraction, 2009.
[20] Y. Zhao, D. Song, S. Wu, S. Xie, H. Wang, M. Wang, W. Zhang, Z. Sun, Y. Ke, S. Wang, W. Huang, R. Fernández, Influence of Fe-rich phases and precipitates on the mechanical behaviour of Al-cu-Mn-Fe-Sc-Zr alloys studied by synchrotron X-ray and neutron, J. Mater. Sci. Technol. 158 (2023) 226–241, https://doi.org/10.1016/j.jmst.2023.03.008.
[21] J. Epp, J. Dong, H. Meyer, A. Bohlen, Analysis of cyclic phase transformations during additive manufacturing of hardenable tool steel by in-situ X-ray diffraction experiments, Scr. Mater. 177 (2020) 27–31, https://doi.org/10.1016/j.scriptamat.2019.09.021.
[22] F.F. Conde, J.D. Escobar, J. Rodriguez, C.R.M. Afonso, M.F. Oliveira, J.A. Avila, Effect of combined tempering and aging in the austenite reversion, precipitation, and tensile properties of an additively manufactured maraging 300 steel, J. Mater. Eng. Perform. 30 (2021) 4925–4936, https://doi.org/10.1007/s11665-021-05553-2.
[23] D. Koutny, D. Skulina, L. Pantělejev, D. Paloušek, B. Lenczowski, F. Palm, A. Nick, Processing of Al-Sc aluminum alloy using SLM technology, in: Procedia CIRP, Elsevier B.V, 2018, pp. 44–48, https://doi.org/10.1016/j.procir.2018.08.027.
[24] Q. Jia, F. Zhang, P. Rometsch, J. Li, J. Mata, M. Weyland, L. Bourgeois, M. Sui, X. Wu, Precipitation kinetics, microstructure evolution and mechanical behavior of a developed Al–Mn–Sc alloy fabricated by selective laser melting, Acta Mater. 193 (2020) 239–251, https://doi.org/10.1016/j.actamat.2020.04.015.
[25] N. Jeyaprakash, C.H. Yang, M.S. Kumar, Influence of coherent intermetallic nano-precipitates on the nano-level mechanical and tribological properties of the laser-powder bed fused Scalmalloy, Mater Charact 193 (2022), https://doi.org/10.1016/j.matchar.2022.112269.
[26] J. Bi, Z. Lei, Y. Chen, X. Chen, Z. Tian, X. Qin, J. Liang, X. Zhang, Effect of Al3(Sc, Zr) and Mg2Si precipitates on microstructure and tensile properties of selective laser melted Al-14.1Mg-0.47Si-0.31Sc-0.17Zr alloy, Intermetallics (Barking) 123 (2020), https://doi.org/10.1016/j.intermet.2020.106822.
[27] R. Vissers, M.A. van Huis, J. Jansen, H.W. Zandbergen, C.D. Marioara, S. J. Andersen, The crystal structure of the β' phase in Al-Mg-Si alloys, Acta Mater. 55 (2007) 3815–3823, https://doi.org/10.1016/j.actamat.2007.02.032.
[28] A.B. Spierings, K. Dawson, P. Dumitraschkewitz, S. Pogatscher, K. Wegener, Microstructure characterization of SLM-processed Al-Mg-Sc-Zr alloy in the heat treated and HIPed condition, Addit. Manuf. 20 (2018) 173–181, https://doi.org/10.1016/j.addma.2017.12.011.
[29] A.B. Spierings, K. Dawson, T. Heeling, P.J. Uggowitzer, R. Schäublin, F. Palm, K. Wegener, Microstructural features of Sc- and Zr-modified Al-Mg alloys processed by selective laser melting, Mater. Des. 115 (2017) 52–63, https://doi.org/10.1016/j.matdes.2016.11.040.
[30] F.F. Conde, J.A. Avila, J.P. Oliveira, N. Schell, M.F. Oliveira, J.D. Escobar, Effect of the as-built microstructure on the martensite to austenite transformation in a 18Ni maraging steel after laser-based powder bed fusion, Addit. Manuf. 46 (2021), https://doi.org/10.1016/j.addma.2021.102122.
[31] J. Zhang, D.F. Chen, C.Q. Zhang, W.S. Hwang, M.R. Han, The effects of heating/cooling rate on the phase transformations and thermal expansion coefficient of C-Mn as-cast steel at elevated temperatures, J. Mater. Res. 30 (2015) 2081–2089, https://doi.org/10.1557/jmr.2015.173.
[32] L.G. de Carvalho, M.S. Andrade, R.L. Plaut, F.M. Souza, A.F. Padilha, A dilatometric study of the phase transformations in 300 and 350 steels during

continuous heating rates, Mater. Res. 16 (2013) 740–744, https://doi.org/10.1590/S1516-14392013005000069.
[33] E. Thronsen, S. Shah, C. Hatzoglou, C.D. Marioara, S. Wenner, S.J. Andersen, B. Holmedal, R. Holmestad, The evolution of precipitates in an Al–Zn–Mg alloy, J. Mater. Res. Technol. 23 (2023) 5666–5680, https://doi.org/10.1016/j.jmrt.2023.02.144.
[34] K. Schmidtke, F. Palm, A. Hawkins, C. Emmelmann, Process and mechanical properties: applicability of a scandium modified Al-alloy for laser additive manufacturing, in: Phys Procedia, Elsevier B.V., 2011, pp. 369–374, https://doi.org/10.1016/j.phpro.2011.03.047.